Diabatic Upwelling in the Tropical Pacific: Seasonal and subseasonal variability

Anna-Lena Deppenmeier,[a] Frank O. Bryan,[a] LuAnne Thompson,[b] William S. Kessler[c]

[a] *NCAR, Boulder, Colorado*

[b] *University of Washington, Seattle, Washington*

[c] *NOAA PMEL, Seattle, Washington*

Corresponding author: Anna-Lena Deppenmeier, deppenme@ucar.edu

ABSTRACT: The equatorial Pacific zonal circulation is composed of westward surface currents, the eastward equatorial undercurrent (EUC) along the thermocline, and upwelling in the eastern cold tongue. Part of this upwelling arises from water flowing along isotherms sloping up to the east, but it also includes water mass transformation and consequent diabatic (cross-isothermal) flow (w_{ci}) that is a key element of surface-to-thermocline communication. In this study we investigate the mean seasonal cycle and subseasonal variability of cross-isothermal flow in the cold tongue using heat budget output from a high resolution forced ocean model. Diabatic upwelling is present throughout the year with surface-layer solar penetration driven diabatic upwelling strongest in boreal spring, and vertical mixing in the thermocline dominating during the rest of the year. The former constitutes warming of the surface layer by solar radiation rather than exchange of thermal energy between water parcels. The mixing driven regime allows heat to be transferred to the core of the EUC by warming parcels at depth. On subseasonal timescales the passage of tropical instability waves (TIWs) enhances diabatic upwelling on and north of the equator. On the equator the TIWs enhance vertical shear and induce vertical mixing driven diabatic upwelling, while off the equator TIWs enhance the sub-5-daily eddy heat flux which enhances diabatic upwelling. Comparing the magnitudes of TIW, seasonal, and interannual w_{ci} variability, we conclude that each timescale is associated with sizeable variance. Variability across all of these timescales needs to be taken into account when modeling or diagnosing the effects of mixing on equatorial upwelling.

1. Introduction

The eastern tropical Pacific plays a major role in global climate variability. Sea surface temperature (SST) variability of the cold tongue couples to the tropical atmosphere via the Bjerknes feedback that can amplify initially small anomalies; it is a fundamental part of the El Niño phenomenon. Cold tongue SST variability thus has global impacts on weather and climate (Alexander et al. 2002; Jong et al. 2016; Yeh et al. 2018; Claar et al. 2018; Cai et al. 2019).

Vertical exchange, from either advection along sloping isopycnals or diapycnal (cross-isopycnal) motion and mixing, can have a large impact on overlying SST by transporting cold waters to the surface. While nearly-continuous measurements of horizontal velocities are available at four moorings along the equator in the Pacific from the Tropical Atmosphere Ocean (TAO) buoy array / the Tropical Pacific Observing System (TPOS) (McPhaden et al. 1998, McPhaden et al. 2010, also see recent review of TPOS by Smith et al. 2019), vertical velocity w is challenging to measure directly. w can be derived from divergence estimates over large control boxes (Wyrtki 1981; Bryden and Brady 1985; Johnson et al. 2001; Meinen et al. 2001) or from moored arrays (Weisberg and Qiao 2000), through a calculation involving small differences between large numbers with resulting large uncertainty (Johnson et al. 2001). Bryden and Brady (1985) use a diagnostic model based on hydrographic sections to derive geostrophic velocity to quantify the three-dimensional circulation in the upper equatorial Pacific. Meinen et al. (2001) use geostrophy and Ekman balance to calculate vertical velocities over a large box spanning the cold tongue. The latter two studies conclude that the diabatic (cross-isothermal) part of the vertical velocity (w_{ci}) is a modest fraction of the total vertical velocity, though the error bars in Meinen et al. (2001) demonstrate the large uncertainty of these observational estimates.

Diabatic processes in the eastern Pacific have been shown to play an important role in driving Warm Water Volume (WWV) variability through diabatic upwelling across the 20°C isotherm, which serves as a proxy for the depth of the thermocline (Meinen and McPhaden 2001; Lengaigne et al. 2012; Huguenin et al. 2020). WWV variability in turn is correlated to the Niño3.4 index at lead times of 3-6 months making it important in ENSO prediction (Meinen and McPhaden 2000; Clarke et al. 2007). Not all studies agree on the contribution of w_{ci} to WWV variability, however. Brown and Federov (2010) and Bosc and Delcroix (2008) argue that w_{ci} varies little interannually. With the current observing array, this important part of the circulation is difficult to constrain.

Here, we make use of a high resolution global ocean model to characterize the diabatic processes and their seasonal and subseasonal variability.

In our previous work we examined the modulation of w_{ci} with the El Niño Southern Oscillation (ENSO) using the saved heat budget from the high resolution global ocean model POP2 at 0.1°horizontal resolution (Smith et al. 2010). We found that the diabatic upwelling across the thermocline is dominated by the vertical heat flux divergence produced by turbulent mixing. Interannual variations in vertical shear between the equatorial undercurrent (EUC) and the south equatorial current (SEC) results in diabatic upwelling being almost entirely shut down during El Niño, and strengthened during La Niña (Deppenmeier et al. 2021).

The tropical Pacific also displays strong seasonal and subseasonal variability that interact with the longer timescales of ENSO (Legeckis 1977; Chelton et al. 2000; Fiedler and Talley 2006; Kessler 2006; Willett et al. 2006). The seasonal cycle of SST in the eastern equatorial Pacific is largely driven by the competing influences of surface fluxes and ocean vertical mixing (Wang and McPhaden 1999; Moum et al. 2013). Using moored platforms for high frequency temperature measurements (χpods) that can be processed to infer the dissipation rate of temperature variance, Moum et al. (2013) show that, on the equator at 140°W, surface heating dominates between February and May, leading to rising SST (Fig. 1a, reproduced from Fig. 3b of Moum et al. (2013)). In contrast, between July and October, turbulent cooling from below exceeds surface heating, leading to a negative SST tendency. Moum et al. (2013) attribute the observed prolonged cooling in September through November to horizontal advection processes not captured by their simplified heat budget depicted in Fig. 1a (Fig.3b of Moum et al. (2013)).

Mixing on the equator is also heavily modulated on subseasonal timescales connected to the passage of Tropical Instability Waves (TIW) (Lien et al. 2008; Moum et al. 2009; Inoue et al. 2012; Holmes and Thomas 2015; Inoue et al. 2019). TIW result from baroclinic and barotropic instabilities in the eastern equatorial current system, and can be detected (e.g. in SST or meridional velocity) as long westward traveling waves with periods between 13-40 days (Legeckis 1977; Miller et al. 1985; Halpern et al. 1988; Qiao and Weisberg 1995). The presence of TIW is strongly modulated by the seasonal cycle (strongest TIW occur during boreal fall and winter, and weaker TIW in boreal spring) and ENSO state (with stronger TIW presence during La Niña than during El Niño conditions). TIW can be detected by examining variability in the appropriate frequency band

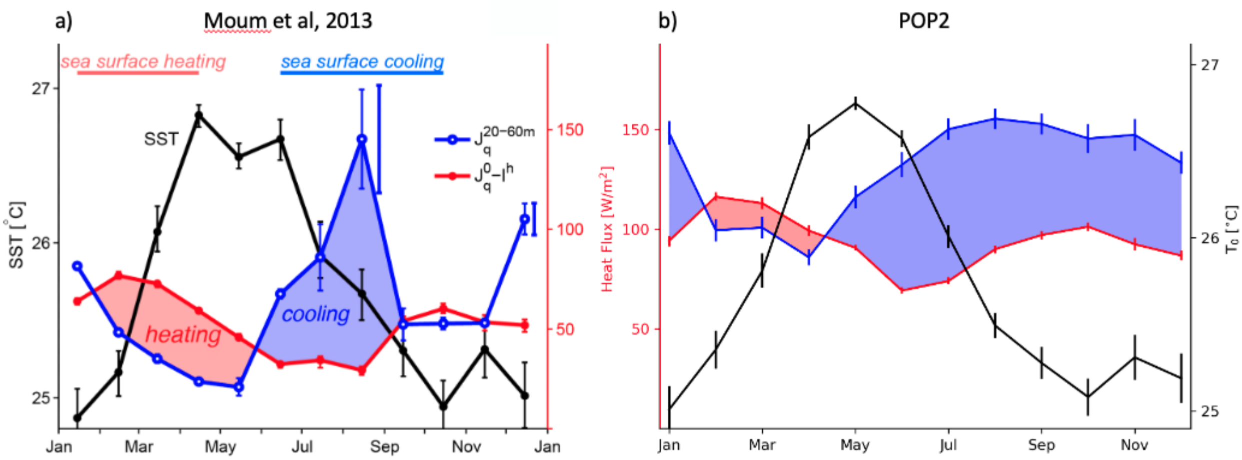

FIG. 1. 2005-2011 mean seasonal cycle of SST (black), turbulent heat flux between 20-60m (J_q, blue), and surface heat flux (SHF, red) at 0°N, 140°W from χPOD data (a, contains gaps (see Moum et al. (2013) Fig. 1f)) and from the POP2 model (b). The error bars on J_q in Fig. 1a correspond to two different ways of estimating the turbulent heat flux, whereas the bars in Fig. 1b show standard deviation.

for a variable that would be influenced by the passage of the TIW, such as variations in meridional velocity. Lien et al. (2008) use a numerical model and Lagrangian floats to show that the leading edge of tropical instability TIW enhances turbulent heat fluxes at the base of surface mixed layer by orders of magnitude. Using χpod measurements, Moum et al. (2009) show that TIWs increase vertical shear in the ocean, resulting in instability and turbulence that cools the surface and warms the EUC waters. Inoue et al. (2012) demonstrate strong modulation of turbulent mixing depending on the phase of a passing TIW which Holmes and Thomas (2015) attribute to increased shear from horizontal vortex stretching. Cherian et al. (2021) demonstrate that a similar mechanism is important off the equator.

Here, we investigate the seasonal cycle and subseasonal variability of w_{ci} and its physical drivers in and across the eastern Pacific cold tongue in a high resolution ocean model.

2. Data Sets and Methodology

a. Model Simulation and Observational Data

We use output from a global 0.1°horizontal resolution POP2 (Parallel Ocean Program version 2) simulation forced with interannually varying JRA55-do surface fluxes with 3 hourly temporal resolution between 1958 and 2018 (Kobayashi et al. 2015; Tsujino et al. 2018) described in Bryan and Bachman (2015) and Deppenmeier et al. (2021). The vertical resolution is 10m in the upper 200m and then increases toward the bottom. The full heat budget averaged over five days during runtime is available for the years 1983-2018. We also use TAO mooring data (Hayes et al. 1991; McPhaden et al. 1998, 2010) provided by the Global Tropical Moored Buoy Array Project Office of NOAA/PMEL for validation of the model simulation along three longitudes that span the cold tongue (170°W, 140°W, 110°W).

Comparing the observational estimate of heat fluxes (Fig. 1a) to POP2 (Fig. 1b) reveals differences in both the surface heating flux (red) as well as the (cooling) turbulent heat flux (blue). The surface heat flux differences stem from differing estimates of the solar penetration flux at the base of the mixed layer and the difference in the net longwave flux (Figs. S1 and S2). This includes a bias in the diagnosis of the solar penetration term, which arises from the POP2 estimates being based on 5 day average output data while the Moum et al. (2013) estimate is based on hourly data. This is not a bias in the model itself, which includes a resolved diurnal cycle of solar heating, but is a limitation of the sampling available for a posteriori analysis.

A comparison of the model time mean and interannual time-scale (1983-2018) vertical structure of temperature and zonal velocity to observations was made in Deppenmeier et al. (2021). The model mean thermocline and the EUC are biased deep, with larger biases at 110°W than at 140°W or 170°W. We found larger biases in the temperature structure (deep thermocline) during La Niña than during El Niño. The model represented the ENSO-cycle variations (anomalies in thermocline and EUC depth and strength) well, again with better representation at 140°W or 170°W than at 110°W.

For the seasonal cycle a comparison of the vertical structure of the model zonal current and temperature to observations shows that the model performs better in the central Pacific than further east (Fig. 2). For the analysis here, we find that the vertical shear above the EUC (above the eastward peak in the zonal velocity) is reasonably well simulated throughout the year, even at 110°W.

POP2 simulates seasonally varying TIW activity, but the TIW kinetic energy is reduced by a factor of two compared to observations (Fig. S3 and S4). This is partly due to weak meridional shear north of the equator due to a weak North Equatorial Countercurrent and a weak South Equatorial

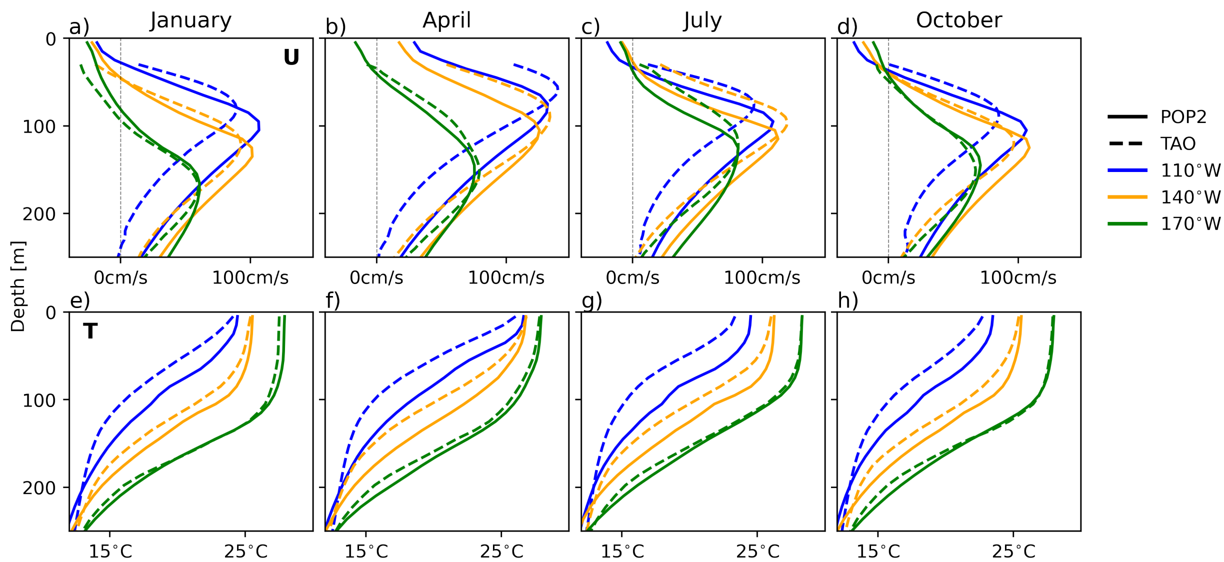

FIG. 2. Seasonal cycle of zonal velocity (upper row) and temperature (lower row), from POP2 (solid lines, 1988-2018 continuous) and the TAO array (dashed lines, 1988-2018, different gaps for different mooring locations) for three different locations.

Current. These biases are attributed to shortcomings in the JRA-55do forcing product (Sun et al. 2019). Additionally, in a forced ocean model the occurrence of TIW does not temporally and spatially align with the imprint the observed TIW left on the forcing field. This misalignment of air-sea fluxes damps the SST anomalies and thus the TIW (Renault et al. 2020; Rai et al. 2021).

b. Water mass transformation framework

Combining the conservation of heat and mass into an equation for water mass transformation allows the calculation of diabatic velocities locally in time and space, and the attribution of the diabatic velocities to specific physical processes, such as vertical mixing, solar penetration, horizontal mixing, and covariance terms. We analyze the rate of water mass transformation with respect to temperature in terms of w_{ci} , movement of a water parcel across an isotherm. The water mass transformation framework has been described in a large body of literature (Walin 1982; Niiler and Stevenson 1982; Nurser et al. 1999; Toole et al. 2004; Hieronymus et al. 2014; Groeskamp et al. 2019). The derivation of the water mass transformation analysis used here is described in Deppenmeier et al. (2021). Our analysis framework is based on the equation for the total diabatic upwelling w_{ci} , which consists of the fluid velocity in the cross-isothermal direction relative to the movement of the isotherms in the same direction (first and second terms, respectively, on the right hand side of first row of equation 1). This is equal to the total derivative of temperature scaled by the magnitude of the temperature gradient, which allows us to attribute the total w_{ci} to physical processes through the heat budget (second row of equation 1).

$$
\begin{aligned}
\overline{w}_{\mathrm{ci}} &\equiv \bar{\mathbf{u}} \cdot \frac{\nabla \overline{T}}{|\nabla \overline{T}|} + \frac{1}{|\nabla \overline{T}|} \frac{\partial \overline{T}}{\partial t} = \frac{1}{|\nabla \overline{T}|} \frac{D\overline{T}}{Dt} \\
&= \frac{1}{\rho_0 c_p |\nabla \overline{T}|} \left[\underset{\substack{\uparrow \\ w_{\mathrm{ci}}^{\mathrm{vmix}}}}{\frac{\partial \bar{J}}{\partial z}} + \underset{\substack{\uparrow \\ w_{\mathrm{ci}}^{\mathrm{solar}}}}{\frac{\partial \bar{I}}{\partial z}} + \underset{\substack{\uparrow \\ w_{\mathrm{ci}}^{\mathrm{hdiff}}}}{\nabla \cdot \overline{\mathbf{H}}_{diff}} - \rho_0 c_p \nabla \cdot \underset{\substack{\uparrow \\ w_{\mathrm{ci}}^{\mathrm{cov}}}}{\left(\overline{\mathbf{u}' T'} \right)} \right] + hot.
\end{aligned}
\tag{1}
$$

The density and specific heat of sea water is given by ρ_0 and c_p respectively, I is the downward radiation flux into the water column as a function of depth z. In the model, the vertical structure of I is based on climatological chlorophyll levels and calculated according to (Ohlmann 2003), see Fig. S1. The parameterized vertical and lateral diffusive heat fluxes are abbreviated with J and $\mathbf{H}_{diff}$, respectively.

Evaluating Eq. 1 using 5-daily averaged terms of the model full heat budget allows calculation of the diabatic component of the vertical circulation (w_{ci}), and importantly also allows us to attribute the cross-isothermal velocities to physical processes such as vertical mixing ($w_{\mathrm{ci}}^{\mathrm{vmix}}$), horizontal mixing ($w_{\mathrm{ci}}^{\mathrm{hdiff}}$), solar penetration ($w_{\mathrm{ci}}^{\mathrm{solar}}$), and sub-5-daily covariance fluxes ($w_{\mathrm{ci}}^{\mathrm{cov}}$). The covariance flux here describes transport by resolved fluctuations on timescales below 5 days. Variability on longer time scales, such as the TIWs, are still mostly resolved after the 5 day averaging. The calculations occur in z-space and the individual terms are then remapped to temperature coordinates by monotonic cubic spline interpolation before further averaging to arrive at the contributions of the different processes to variations of w_{ci} on particular timescales.

The attribution of w_{ci} to physical processes such as solar penetration and vertical mixing depends on the divergence (vertical derivative) of those heat fluxes. Thus, peak w_{ci} does not necessarily coincide with peak heat flux, but instead with its maximum vertical gradient. For solar penetration, the downward flux reduces monotonically with depth: its divergence maintains one sign, and $w_{\mathrm{ci}}^{\mathrm{solar}}$ is always positive (i.e. warming parcels, moving them from colder to warmer classes, Fig. 3b). This warming is not necessarily reflected in a spatial movement of water parcels, rather the cross-isothermal velocity can also result from warming of a parcel in place. In this case, the isotherm shifts relative to the parcel.

In the eastern Pacific cold tongue, vertical mixing is closely connected to the destabilizing shear between the eastward EUC and overlying westward South Equatorial Current (SEC) (Fig. 2, Sun et al. 1998; Smyth and Moum 2013; Smyth et al. 2013). The resulting heat flux from mixing J also depends on the temperature gradient, which is large above the thermocline but much smaller in the roughly 50m thick surface mixed layer (Fig. 2, noting that instantaneous mixed layer thickness can be larger than these seasonal averages). Thus J owing to vertical mixing peaks near the base of the mixed layer so its divergence takes both signs (Fig. 3b and c, see also Fig.7 in Deppenmeier et al. 2021). $w_{\mathrm{ci}}^{\mathrm{vmix}}$ is large and positive (warming) from the EUC core to about 50m depth, then negative above, where shallow water parcels are cooled by mixing with more heat removed from below.

The combined impact of $w_{\mathrm{ci}}^{\mathrm{solar}}$ and $w_{\mathrm{ci}}^{\mathrm{vmix}}$ is to deliver solar heating down to the thermocline level, much below the penetration depth of solar radiation (Fig. 3c).

Since w_{ci} is by definition perpendicular to isotherms, in the mixed layer, where the temperature gradient is more horizontal (meridional) rather than vertical; w_{ci} can be dominantly in the poleward direction (Fig. 3a).

3. Results

The seasonal evolution of SST and its drivers in the model is similar in character to that inferred from the Moum et al. (2013) measured temperature variance at 140°W, with timing of the transition from a surface flux dominated heat budget to a vertical turbulent flux dominated heat budget occurring at the same time of year as in the observations (compare Figs. 1a and b). During September-November however, in the model strong turbulent heat fluxes occurs (cooling) while the SST is relatively constant (Fig. 1b) while observational results suggests weak turbulent heat fluxes during this time (Fig. 1a). Both surface and turbulent terms remain large in the model representation at this time (Figs. 1b). Moum et al. (2013) suggested that horizontal advection

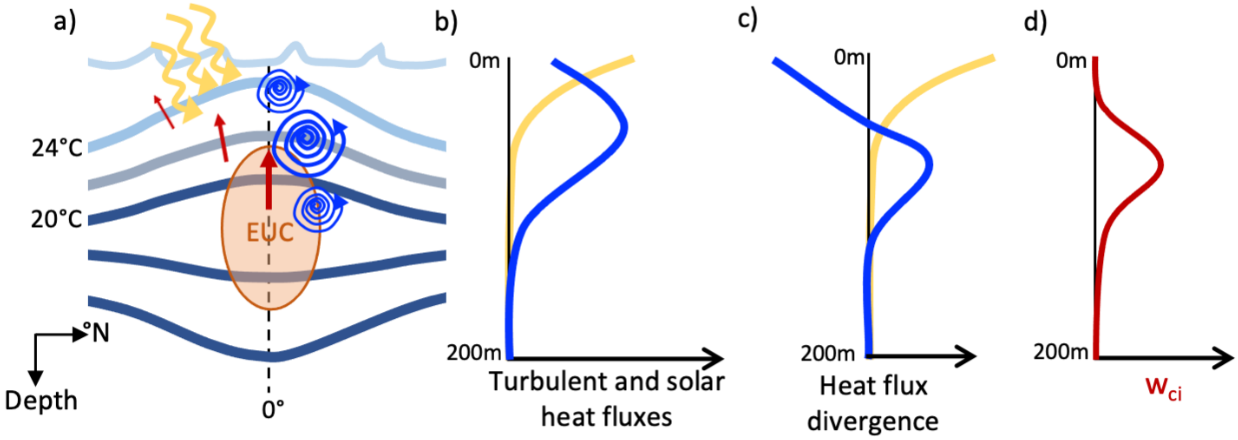

FIG. 3. Schematic of representative cross-equatorial structure in the cold tongue. Isotherms are represented by the blue lines with darker shades of blue indicating colder water. Solar heat flux (I; yellow arrows and profile) is maximum at the surface and decreases with depth. Heat flux due to turbulent mixing (J; blue swirls and profile) is large in the high shear, high temperature gradient region above the EUC, then decreases in the surface mixed layer. w_{ci} is proportional to the vertical gradient of these fluxes. Red arrows show total w_{ci} (in the direction of the temperature gradient). Turbulent mixing, solar penetration and w_{ci} are active on and across the equator.

might be significant at this time, but noted the difficulty in estimating horizontal SST gradients consistent with the measured currents that are reliable only below 25m in depth.

a. The seasonal cycle of w_{ci}

The diabatic upwelling w_{ci} in the tropical Pacific cold tongue thermocline exhibits a distinct seasonal cycle (Fig. 4). The seasonally varying thermocline w_{ci} , defined as the monthly average w_{ci} between 20 and 24°C, indicates that the strongest water mass transformation from below-thermocline to near-surface waters takes place between boreal summer and winter, and is reduced in boreal spring.

In all seasons, the largest values of w_{ci} in the thermocline are found east of 155°W (Fig. 4) and are concentrated near the equator. The latitudinal extent of these large values of w_{ci} has large temporal variability. Notably, w_{ci} is confined closely to the equator in April, whereas it extends 2°away from the equator in both hemispheres in the other seasons.

While the region of large w_{ci} in the thermocline is much reduced in April (Fig. 4b), there is equatorial diabatic upwelling in the water column throughout the year. However, it occurs above

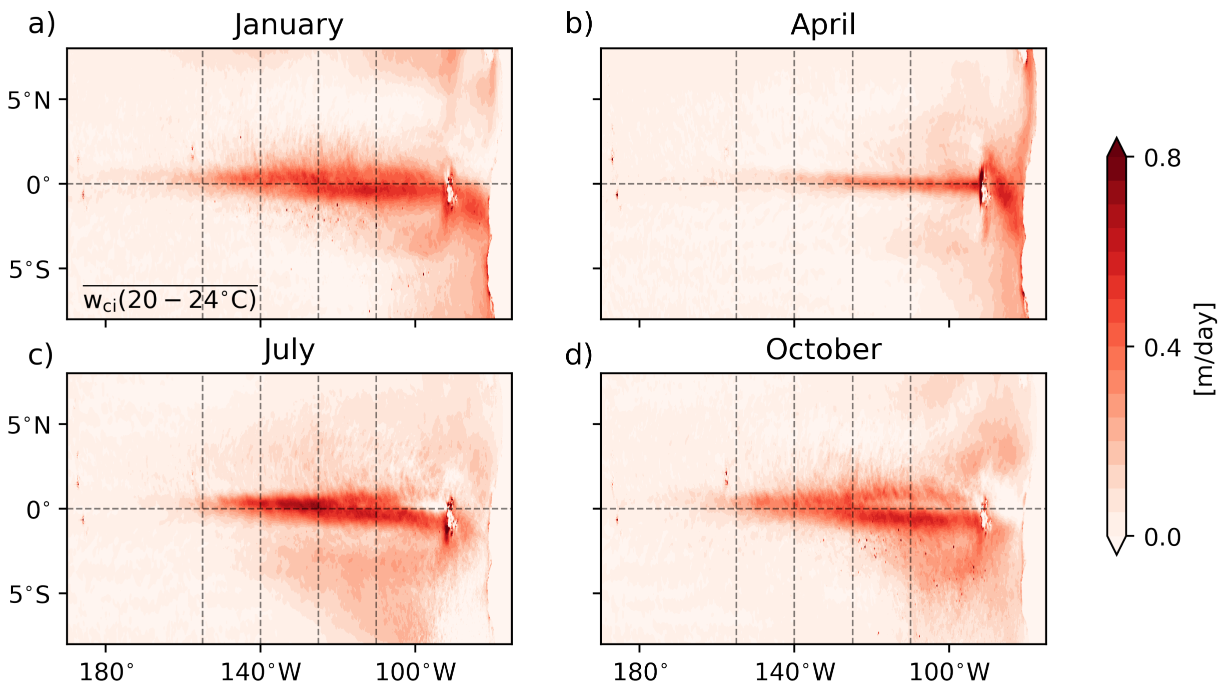

FIG. 4. Seasonally stratified mean thermocline diabatic upwelling (approximated by averaging over 20-24°C). Stippled vertical lines indicate the locations of the TAO moorings, 155°W, 140°W, 125°W and 110°W.

the thermocline (Fig. 5d) where w_{ci} is predominantly horizontal. Temperatures above the 24°C isotherm are more likely to be in the mixed layer rather than in the thermocline (Fig. 6c, f, i).

To understand the variability of thermocline diabatic upwelling we decompose w_{ci} into its physical processes according to Eq. 1 (bottom row, see discussion in Section 2b) along 140°W. The signal of w_{ci} throughout the seasonal cycle, much like on interannual time scales (Deppenmeier et al. 2021), is dominated by two physical drivers: vertical mixing (Fig. 5, center column) and solar penetration (Fig. 5, right column).

In the mixed layer near the surface (also indicated through its proximity to the hatching in Fig. 5), the warming effect of solar penetration (Fig. 5c, f, i, l) dominates w_{ci} . Close to the surface $w_{\mathrm{ci}}^{\mathrm{vmix}}$ is less than zero as the divergence of the vertical mixing induced turbulent heat flux cools water parcels by mixing out more heat at the bottom of a parcel than mixing in at the top of the parcel. However, the magnitude of $w_{\mathrm{ci}}^{\mathrm{vmix}}$ is less than that of $w_{\mathrm{ci}}^{\mathrm{solar}}$ resulting in a net warming in the mixed layer (w_{ci} ¿0).

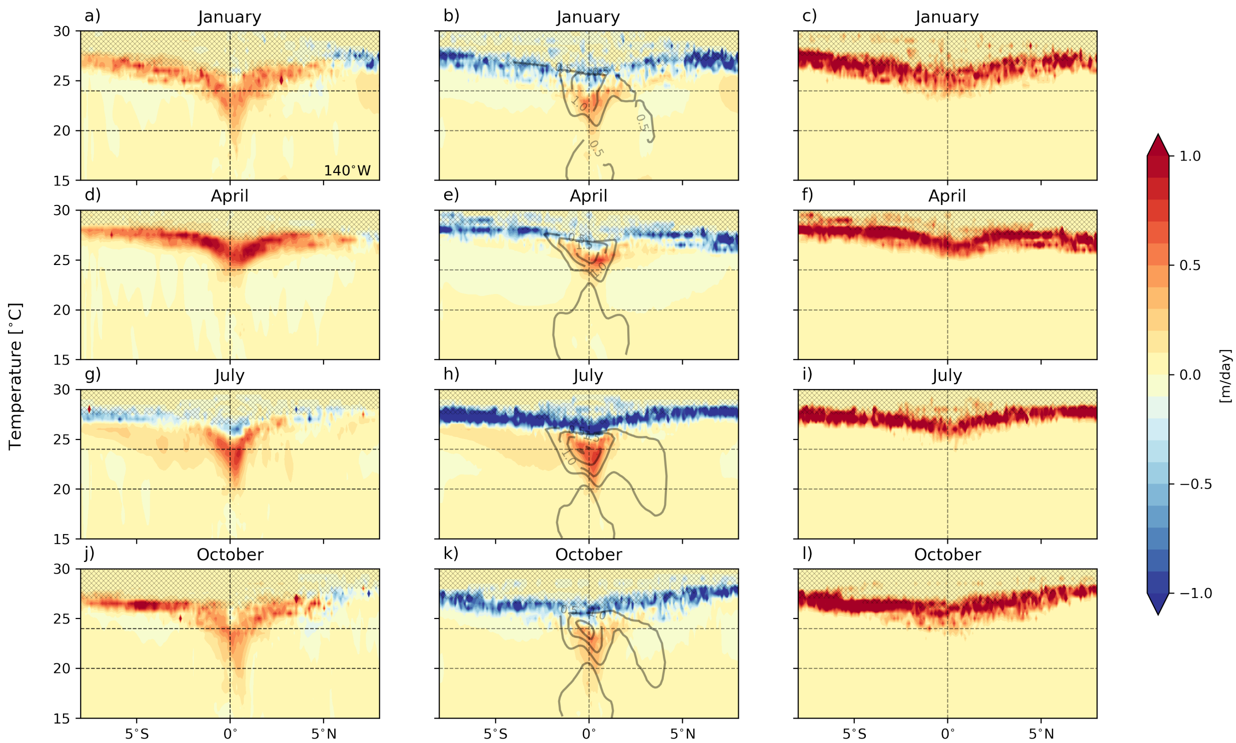

FIG. 5. Seasonally stratified cross-equatorial cross sections of diabatic upwelling according to Eq. 1 along 140°W: total (left column), induced by vertical mixing (center column) and solar penetration (right column). Text insets are the average total diabatic upwelling on the equator at 140°W. Hatching indicates that the isotherm is present less than 50% of the time. Contours in the central column indicate absolute vertical shear. Horizontal dashed lines indicate that 20°C and 24°C isotherms.

Below the mixed layer $w_{\mathrm{ci}}^{\mathrm{vmix}}$ is positive and dominates w_{ci} (Fig. 5, b, e, h, k). $w_{\mathrm{ci}}^{\mathrm{vmix}}$,and therefore w_{ci} , extends well into the thermocline to temperatures below 20°C in July and October while it is confined to the temperatures above 24°C in April.

We find that interannual w_{ci} variability is driven by $w_{\mathrm{ci}}^{\mathrm{vmix}}$, which is modulated by changes in vertical shear (Deppenmeier et al. 2021). Strong vertical shear in the upper ocean also coincides with w_{ci} on the seasonal time scale. Diabatic upwelling resulting from increased vertical shear induced mixing on seasonal time scales is similar to what we see on interannual time scales (Deppenmeier et al. 2021, Fig. 5b, e, h, k). The depth and temperature of the water column to which w_{ci} is controlled by the vertical shear is associated with the EUC. In April, (Fig. 5e) the vertical shear extends only slightly below the 24°C isotherm, and therefore $w_{\mathrm{ci}}^{\mathrm{vmix}}$ and w_{ci} are

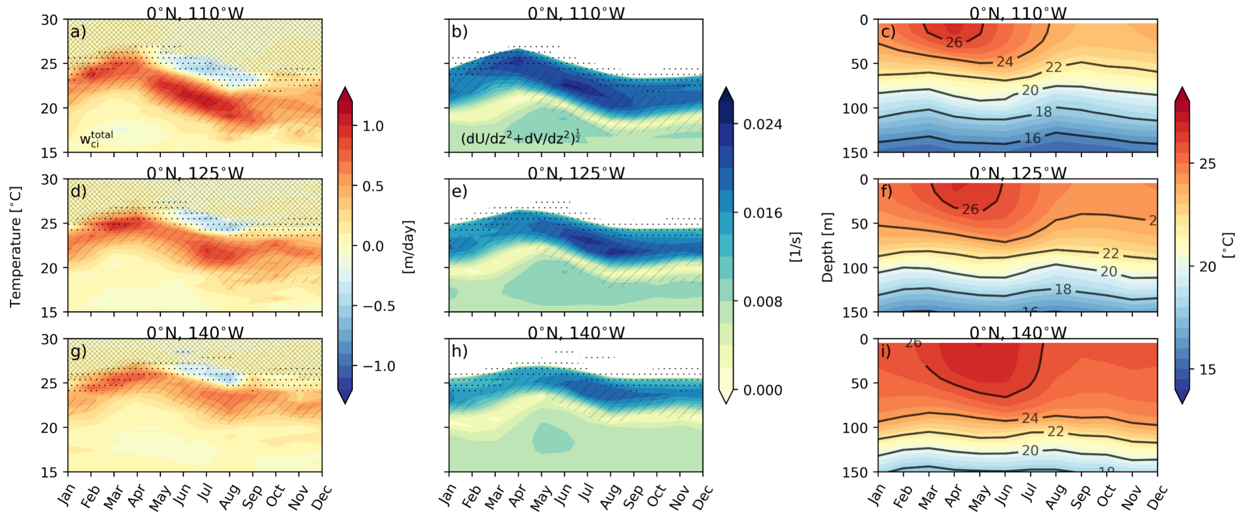

FIG. 6. Seasonal cycle of total diabatic upwelling (w_{ci} , a, d, g), vertical shear (b, e, h), and temperature (c, f, i) for three different longitudes in the cold tongue along the equator. The strength of the contribution of solar and vertical mixing induced diabatic w_{ci} is indicated by dots (solar higher than 0.3m/day) and slashes (vertical mixing higher than 0.3m/day). Note that w_{ci} and absolute vertical shear are shown in temperature coordinates, while the temperature is shown in depth coordinates.

confined to waters warmer than 24°C. The shear is mostly controlled by the zonal component of the velocity, the vertical shear of the meridional component of the velocity is an order of magnitude smaller (not shown). While the EUC is strongest and shallowest in spring, during that time the trade winds relax and the SEC retreats; the surface flow at 140°W becomes eastward (Fig. 2b). As a result, the vertical shear occurs near the surface where the water is close to 26°C (Figs. 2f and 6).

b. Zonal dependence of seasonal diabatic upwelling

The evolution of diabatic upwelling w_{ci} in the Eastern Pacific along the equator is similar at 110°W, 125°W and 140°W (Fig. 6). The total diabatic upwelling w_{ci} (colors, Fig.6 a, d, g) is stronger in the east (110°W, Fig. 6a) and weakens toward the west (140°W, Fig. 6g). Consistent with the increase of SST to the west along the equator (Fig. 6c, f, i), the maximum w_{ci} occurs at warmer temperatures in the west than in the east.

At 110°W, 125°W and 140°W, two w_{ci} maxima exist in the year: one between June and September, and one between February and April (Fig. 6a, d, and g). The bulk of the diabatic upwelling is driven by vertical mixing which is modulated by the seasonal cycle of vertical shear(Fig. 6 b, e, h). In boreal summer (JJA) the maxima in w_{ci} occur at the same time as maxima in vertical shear for all longitudes. Note that it is the vertical derivative of the turbulent heat flux J which impacts $w_{\mathrm{ci}}^{\mathrm{vmix}}$, which is in turn impacted by the derivative of the shear and not the absolute strength of vertical shear (Fig. 6 b, e, h).

Between February and April, however, the second maxima of w_{ci} at 125°W and 140°W does not correspond to a maxima in shear (Fig. 6d and e; g and h). Instead, during these months large w_{ci} maxima occurs in warmer temperature classes during the time of the large contribution from solar penetration (dots in Fig. 6).

We conclude that there are two regimes of diabatic upwelling over the seasonal cycle on the equator: in February to April, solar penetration contributes to water mass transformation in warm temperature classes close to the surface (solar regime). In all other months, vertical mixing driven by the mean vertical shear of the EUC enables diabatic upwelling. The temperatures in which w_{ci} are active in the solar driven regime are warm and above the thermocline. This w_{ci} is hence better understood as an intensification of poleward water mass transformation, rather than strong diabatic upwelling in the vertical.

c. Tropical Instability Waves impact on w_{ci}

On subseasonal scales, there is evidence that TIWs assert a rectified effect on the diabatic limb of the upwelling on the equator and to the north. We demonstrate this for an example year (2010), for which we show hovmoeller diagrams of time against longitude for SST together with TIW kinetic energy, w_{ci} , $w_{\mathrm{ci}}^{\mathrm{vmix}}$, and $w_{\mathrm{ci}}^{\mathrm{cov}}$ at 2°N and on the equator (Figs. 7 and 8). The TIW kinetic energy is found by bandpass filtering meridional velocity between 12 and 33 days. The resulting anomalies are squared, then lowpass filtered for time scales longer than 20 days (following Warner and Moum (2019)). The hovmoeller diagram of SST along 2°N shows that TIWs occur in all months but March-May with alternating bands of warm and cold SST traveling westward as time progresses (Fig. 7a). The TIW kinetic energy at 2°N, 125°W shows that TIWs are nearly absent in boreal spring, and are present from July through December, peaking in December (Fig. 7a). SST (Fig. 7a) show evidence of westward propagation as does diabatic upwelling (between 20-22°C,

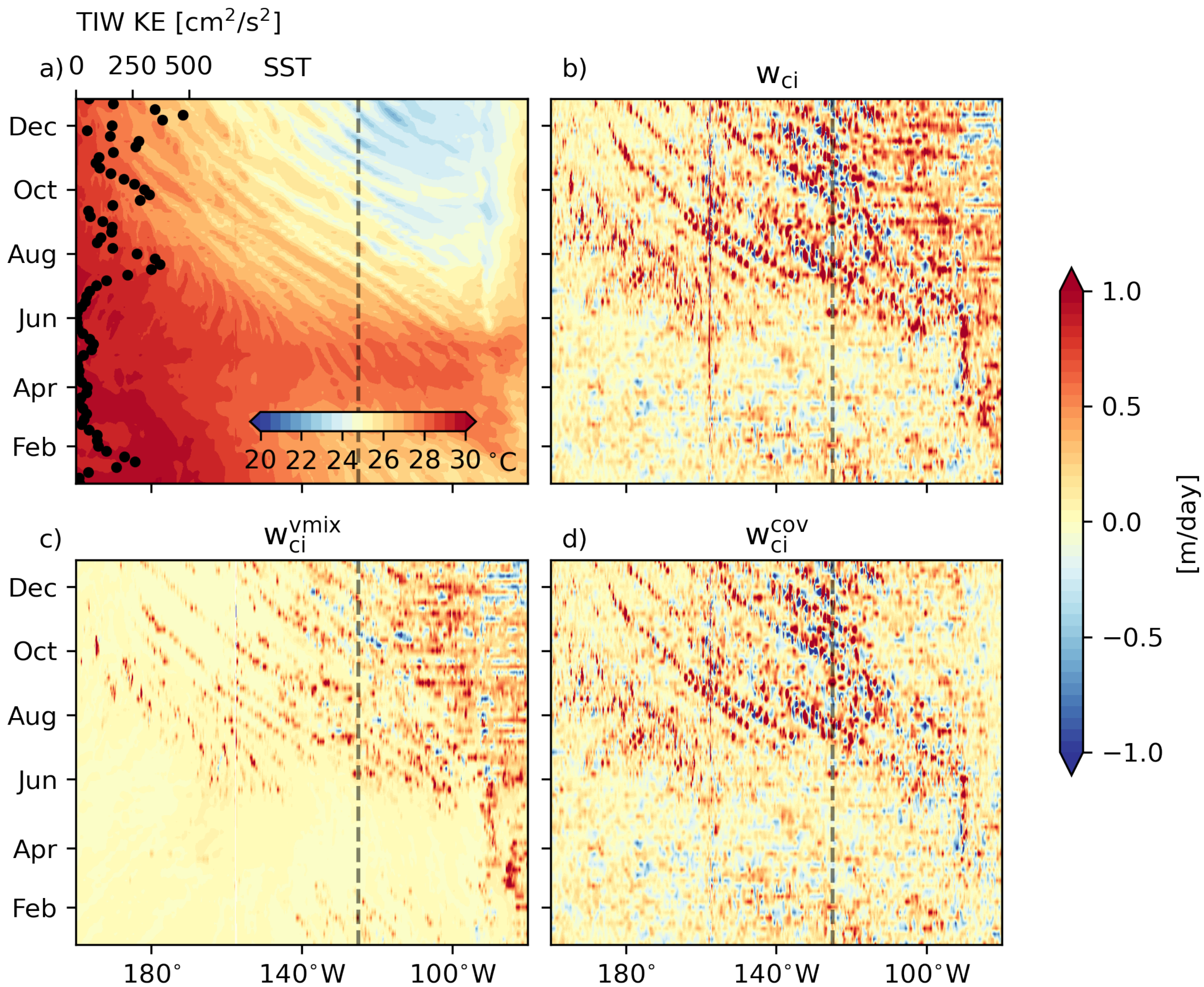

FIG. 7. Hovmoeller diagrams of sea surface temperature (a), total diabatic upwelling w_{ci} (b), vertical mixing driven diabatic upwelling $w_{\mathrm{ci}}^{\mathrm{vmix}}$ (c), and diabatic upwelling driven by covariance on time scales under 5 days $w_{\mathrm{ci}}^{\mathrm{cov}}$, d) along 2°N for 2010. All diabatic upwelling quantities are averaged over the 20-22°C isotherms (not sensitive to averaging within the thermocline). All fields depicted in color are unfiltered from the 5 daily output. TIW kinetic energy estimated at 2°N, 125°W is indicated as dots in a).

Fig. 7b). The streaks of w_{ci} overlap with the TIW induced streaks of cool SSTs, indicating that TIW enhance local w_{ci} , particularly during their cold phase.

The diabatic upwelling signal stems from both the mixing $w_{\mathrm{ci}}^{\mathrm{vmix}}$ (Fig. 7c) and covariance $w_{\mathrm{ci}}^{\mathrm{cov}}$ components in Eq 1. The covariance component $w_{\mathrm{ci}}^{\mathrm{cov}}$ results from the covariance on sub 5-day time scales that results from the passage of a TIW front. This could be an indication of short lived frontal circulations (Perez et al. 2010) and their impact on w_{ci}. On the equator, TIW related streaks can also be seen in w_{ci}, but are less distinct than variability of w_{ci} associated with the seasonal cycle (Fig. 8). Here, most of the signal corresponding to TIW passage can be found in the $w_{\mathrm{ci}}^{\mathrm{vmix}}$ component (Fig. 8c), rather than in the covariance component (Fig. 8d). Thus, the passage of TIWs intensifies the diabatic upwelling both on and off the equator. However, the physical drivers of the intensification is different depending on the location. This mechanism is the subject of a future study.

d. Diabatic upwelling variability across time scales

This study and the results in Deppenmeier et al. (2021) demonstrate that diabatic upwelling is strong throughout the eastern tropical Pacific and varies on subseasonal to interannual time scales. We see comparable amplitude of w_{ci} variability for subseasonal (specifically TIW modulated), seasonal, and interannual (ENSO) time scales (Fig. 9a, b, c). For the subseasonal (TIW) time scale we separately examine high and low TIW kinetic energy periods using a 200cm^2/s^2 threshold (the results are insensitive within the cutoffs of 150cm^2/s^2 to 250cm^2/s^2). For the interannual time scale we define La Niña and El Niño phases via Niño3.4 SST anomalies that exceed ±0.4°C for at least six months (Deppenmeier et al. 2021).

Large diabatic upwelling in the seasonal cycle occurs in two regimes. In March, the shallow maximum near 25°C reflects primarily solar penetration (Figs. 6d and 9a) during this season of weak cloudiness (Klein and Hartmann 1993; Yu and Mechoso 1999; Xu et al. 2005). In all other seasons maximum diabatic upwelling occurs near 22°C below most of the solar influence and just above the thermocline, driven by vertical mixing (Figs. 6e and 9a). Both these seasonal maxima are comparable to or larger than the ENSO or TIW peaks (compare Figs.9a, b, c).

As the thermocline and EUC begin to deepen in early boreal summer, strong shear squared S^2 becomes large at shallow depths and vertical mixing dominates in the otherwise solar-influenced upper region of the water column. $w_{\mathrm{ci}}^{\mathrm{vmix}}$ acts to oppose the solar warming, cooling the uppermost layer strongly resulting in negative w_{ci} in July (Fig. 9a). Below the solar dominated surface layer, near 22°C, the seasonal variation of w_{ci} is primarily driven by variation of the S^2 above the EUC. From about June through the end of the year S^2 at these depths is strong (Fig. 6e), corresponding to strong mixing-driven w_{ci}.

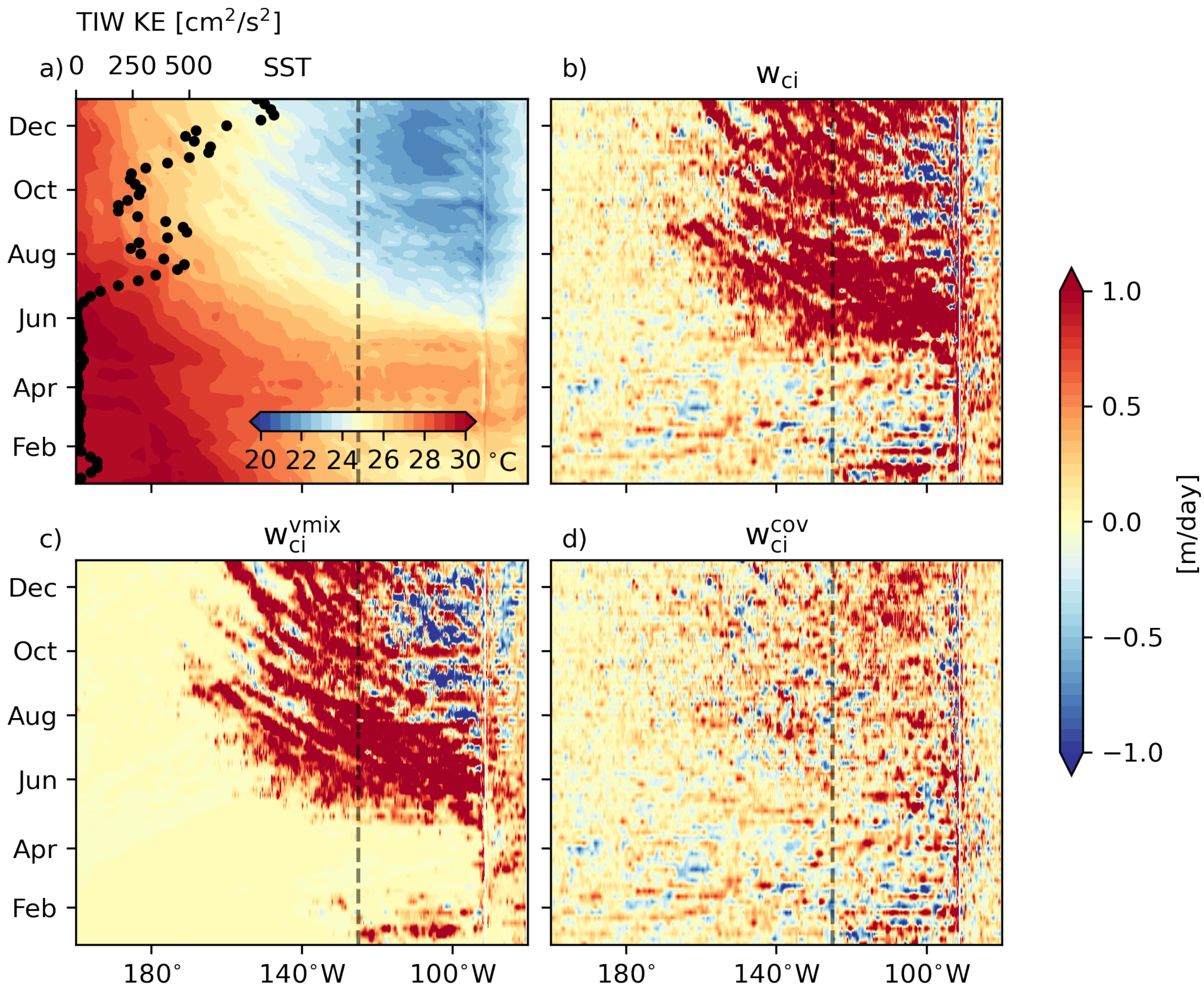

FIG. 8. Hovmoeller diagrams of sea surface temperature (a), total diabatic upwelling w_{ci} (b), vertical mixing driven diabatic upwelling w_{ci}^{vmix} (c), and diabatic upwelling driven by covariance on time scales under 5 days w_{ci}^{cov} , d) along 0°N for 2010. All diabatic upwelling quantities are averaged over the 20-22°C isotherms (not sensitive to averaging within the thermocline). All fields depicted in color are unfiltered from the 5 daily output. TIW kinetic energy estimated at 0°N, 125°W is indicated as dots in a).

We show that increased S^2 also contributes to increased vertical-mixing-driven w_{ci}^{vmix} for TIW conditions: during periods of high TIW kinetic energy stronger w_{ci} (Fig. 9d) occurs coinciding with strong S^2 (Fig. 9e). The differences in w_{ci} are statistically significant at the 99% confidence interval (estimated via Welch's t-test). The hovmoeller diagrams in Fig. 7 and Fig. 8 demonstrate that TIWs modulate diabatic upwelling. This effect can be quantified by comparing profiles of

w_{ci} split by high and low TIW kinetic energy (Fig. 9c). Instances of high TIW kinetic energy coincide with stronger diabatic upwelling in the water column. We examine w_{ci} related to TIW kinetic energy variability across the entire year (dashed) and for boreal fall, SON (solid, Fig. 9c). We add the differences between the high and low TIW KE within a season (SON) to avoid folding the seasonal cycle into the subseasonal cycle analysis. We choose SON because high TIW activities occur in two thirds of the 5-day averaged fields, and are low for the rest of the time period. We find that w_{ci} is significantly stronger during periods of high TIW kinetic energy both for a given season (SON), and throughout the year (Fig. 9c).

During La Niña conditions w_{ci} has values as large as 0.6 m/day while during El Niño conditions w_{ci} maxima are only about half as big and occur at warmer temperatures (Fig. 9b). It is noteworthy that the timescales we investigate are connected. TIW occurrence varies both seasonally and interannually, being practically absent in March-May and during El Niño, and enhanced during Sep-Feb and during La Niña. Similarly, ENSO evolution is also connected to the seasonal cycle. Whether TIW dominantly influence the variability we see on other time scales is a matter of active research.

To place the w_{ci} variability in context we compare it to SST variability across the time scales (Fig. 9f). SST variability is largest (by construction) between ENSO phases (the Niño3.4 index exceeds ± 0.4 for several months). This is followed by the strength of the variability of the seasonal cycle, which displays the largest variability in S^2 and w_{ci} . TIW phases also strongly influence SST, with low TIW kinetic energy usually being accompanied by warmer temperatures and high TIW kinetic energy by colder temperatures. We do not find a one to one relationship between the strength of w_{ci} variability and SST variability for these difference processes.

4. Conclusion

Diabatic upwelling w_{ci} varies across time scales. Most noticeably, large variations in w_{ci} are seen in the seasonal cycle. In all seasons but March, April, May (MAM) the maximum in w_{ci} is driven solely by vertical mixing induced by the strong vertical shear above the equatorial undercurrent. In MAM, w_{ci} is confined to warm temperature classes, and solar penetration dominates. In these warm temperature classes positive w_{ci} consists of poleward watermass transformation in the mixed layer - equivalent to solar heating shifting warmer isotherms towards the equator - rather than $w_{\mathrm{ci}}^{\mathrm{vmix}}$'s vertical motion found in the upper thermocline.

While most of the seasonal cycle variability can be explained by changes in the seasonal mean quantities, such as differences in S^2, the results here suggest that TIWs can rectify to induce seasonal variations in w_{ci} . Part of this signal contained in the vertical mixing component induced by eddy stirring, and part of it appears as the covariance term in Eq. 1 from covariability of velocity and temperature during the passage of a TIW. Strengthened turbulent heat fluxes during the passage of TIWs have also been described by Lien et al. 2008; Moum et al. 2009; Inoue et al. 2012; Holmes and Thomas 2015 on the equator and Cherian et al. 2021 off the equator. Here, we find evidence that passing TIW rectify to create diabatic upwelling that results in increased water mass transformation on the equator.

Observations of vertical mixing are clearly important to understand all components of the tropical Pacific circulation and heat budget. Here we demonstrate that the impact of vertical mixing variability on diabatic upwelling is not dominated by a specific timescale, rather there is sizeable variability at each of the subseasonal, seasonal, and interannual timescales. Our estimate of diabatic upwelling is based on a model simulation which captures the main aspects of the circulation reasonably well, but also displays some biases such as the a too deep thermocline and weak TIW kinetic energy. This highlights the importance of observationally constraining the diabatic component of the tropical Pacific circulation and underscores the need for targeted observational efforts.

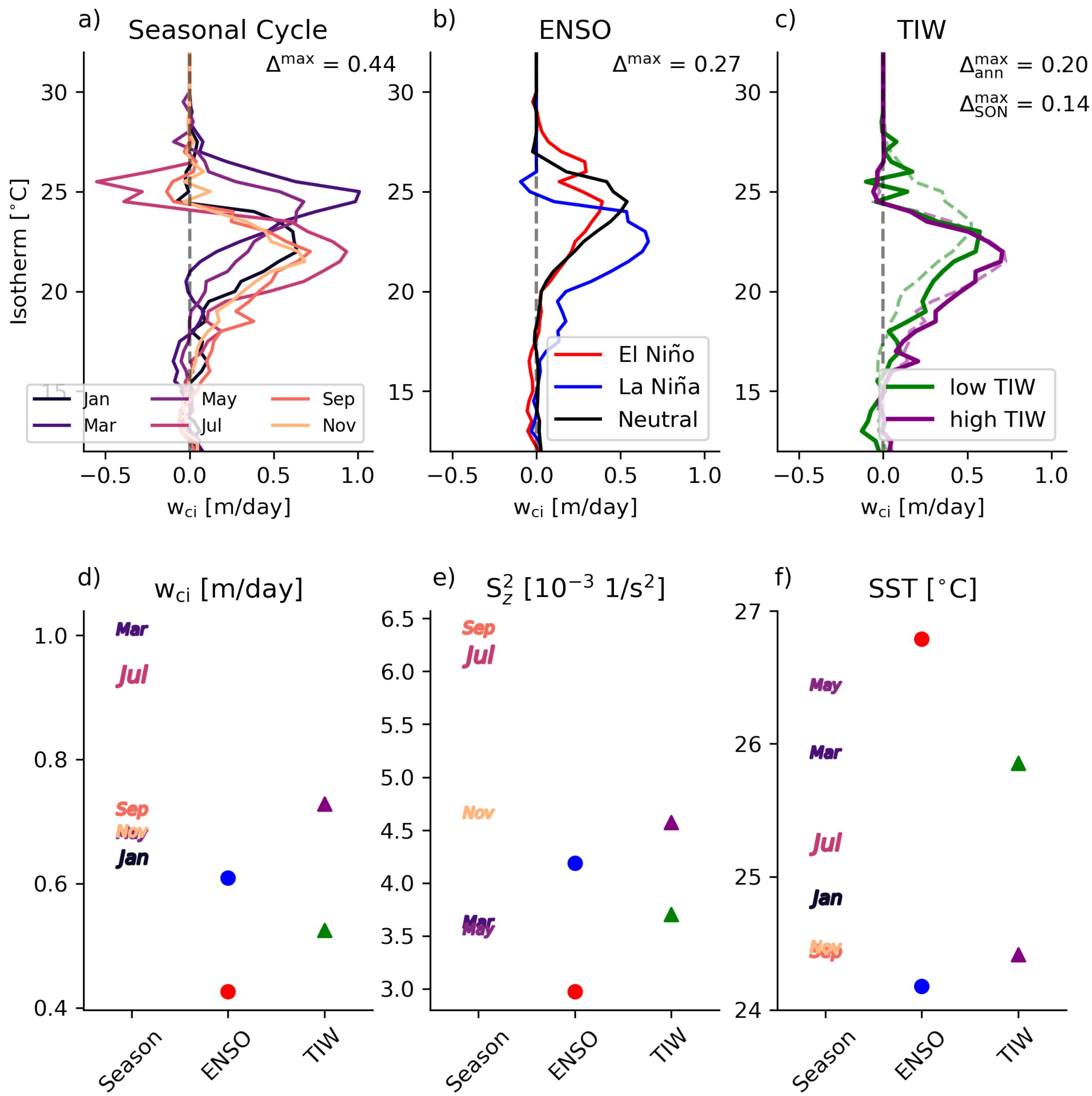

FIG. 9. Profiles of total diabatic upwelling w_{ci} at 0°N, 125°W averaged over different time scales: a) the climatological seasonal cycle, b) El Niño, La Niña, and Neutral ENSO conditions, c) high and low TIW kinetic energy (TIW KE), both for the whole year (dashed), and for SON months only (solid). Maximum w_{ci} in the column (d) for the seasonal cycle (letters), high and low TIW KE (triangles), and ENSO phases (dots), maximum shear in the column split by time scales (e), and mean SST for the different time scales (f). Symbols are color coded as in the legend in row 1 the same for d, e, and f.

Acknowledgments. This study was supported by the National Center for Atmospheric Research, which is a major facility sponsored by the National Science Foundation under Cooperative Agreement No. 1852977, and by the NOAA Climate Variability Program under Grant Agreement No. NA18OAR4310399. LT was supported by NOAA Climate Variability Program under Grant Agreement NA18OAR4310400. This work is part of the CVP TPOS 2020 pre-field modeling effort led by Dr. Sandy Lucas, and is PMEL contribution number 5336. Computing resources were provided by the Climate Simulation Laboratory at NCAR's Computational and Information Systems Laboratory (CISL). TAO observational data were made available by the GTMBA Project Office of NOAA/PMEL and accessed through the website `https://www.pmel.noaa.gov/tao/drupal/disdel/`. The analysis benefited from the open source packages dask (Rocklin 2015), xarray (Hoyer and Hamman 2017) and xgcm (Abernathy et al. 2020).

Data availability statement. The data underlying the final figures in this manuscript will be made available via https://zenodo.org/ upon acceptance, when we know what the final figures will be. TAO observational data can be accessed through https://www.pmel.noaa.gov/tao/drupal/disdel/.

References

Abernathy, R., and Coauthors, 2020: xgcm. **v0.6.0**, https://doi.org/10.5281/zenodo.5752560.

Alexander, M. A., I. Bladé, M. Newman, J. R. Lanzante, N.-C. Lau, and J. D. Scott, 2002: The atmospheric bridge: The influence of enso teleconnections on air–sea interaction over the global oceans. *Journal of climate*, **15 (16)**, 2205–2231.

Bosc, C., and T. Delcroix, 2008: Observed equatorial rossby waves and enso-related warm water volume changes in the equatorial pacific ocean. *Journal of Geophysical Research: Oceans*, **113 (C6)**.

Brown, J., and A. Federov, 2010: Estimating the diapycnal transport contribution to warm water volume variations in the tropical pacific ocean. *Journal of Climate*, **23**, 221–237.

Bryan, F., and S. Bachman, 2015: Isohaline salinity budget of the north atlantic salinity maximum. *Journal of Physical Oceanography*, **45 (3)**, 724–736.

Bryden, H. L., and E. C. Brady, 1985: Diagnostic model of the three-dimensional circulation in the upper equatorial pacific ocean. *Journal of Physical Oceanography*, **15 (10)**, 1255–1273.

Cai, W., and Coauthors, 2019: Pantropical climate interactions. *Science*, **363 (6430)**.

Chelton, D. B., F. J. Wentz, C. L. Gentemann, R. A. de Szoeke, and M. G. Schlax, 2000: Satellite microwave sst observations of transequatorial tropical instability waves. *Geophysical Research Letters*, **27 (9)**, 1239–1242.

Cherian, D., D. Whitt, R. Holmes, R.-C. Lien, S. Bachman, and W. Large, 2021: Off-equatorial deep-cycle turbulence forced by tropical instability waves in the equatorial pacific. *Journal of Physical Oceanography*, **51 (5)**, 1575–1593.

Claar, D. C., L. Szostek, J. M. McDevitt-Irwin, J. J. Schanze, and J. K. Baum, 2018: Global patterns and impacts of el niño events on coral reefs: A meta-analysis. *PLoS One*, **13 (2)**, e0190 957.

Clarke, A. J., S. Van Gorder, and G. Colantuono, 2007: Wind stress curl and enso discharge/recharge in the equatorial pacific. *Journal of Physical Oceanography*, **37 (4)**, 1077–1091.

Deppenmeier, A.-L., F. O. Bryan, W. S. Kessler, and L. Thompson, 2021: Modulation of cross-isothermal velocities with enso in the tropical pacific cold tongue. *Journal of Physical Oceanography*, **51 (5)**, 1559–1574.

Fiedler, P. C., and L. D. Talley, 2006: Hydrography of the eastern tropical pacific: A review. *Progress in Oceanography*, **69 (2-4)**, 143–180.

Groeskamp, S., S. M. Griffies, D. Iudicone, R. Marsh, A. G. Nurser, and J. D. Zika, 2019: The water mass transformation framework for ocean physics and biogeochemistry. *Annual review of marine science*, **11**, 271–305.

Halpern, D., R. A. Knox, and D. S. Luther, 1988: Observations of 20-day period meridional current oscillations in the upper ocean along the pacific equator. *Journal of Physical Oceanography*, **18 (11)**, 1514–1534.

Hayes, S., L. Mangum, J. Picaut, A. Sumi, and K. Takeuchi, 1991: Toga-tao: A moored array for real-time measurements in the tropical pacific ocean. *Bulletin of the American Meteorological Society*, **72 (3)**, 339–347.

Hieronymus, M., J. Nilsson, and J. Nycander, 2014: Water mass transformation in salinity–temperature space. *Journal of Physical Oceanography*, **44 (9)**, 2547–2568.

Holmes, R. M., and L. N. Thomas, 2015: The modulation of equatorial turbulence by tropical instability waves in a regional ocean model. *Journal of Physical Oceanography*, **45 (4)**, 1155–1173.

Hoyer, S., and J. Hamman, 2017: xarray: N-D labeled arrays and datasets in Python. *Journal of Open Research Software*, **5 (1)**, https://doi.org/10.5334/jors.148, URL http://doi.org/10.5334/jors.148.

Huguenin, M. F., R. M. Holmes, and M. H. England, 2020: Key role of diabatic processes in regulating warm water volume variability over enso events. *Journal of Climate*, **33 (22)**, 9945–9964.

Inoue, R., R.-C. Lien, and J. Moum, 2012: Modulation of equatorial turbulence by a tropical instability wave. *Journal of Geophysical Research: Oceans*, **117 (C10)**.

Inoue, R., R.-C. Lien, J. N. Moum, R. C. Perez, and M. C. Gregg, 2019: Variations of equatorial shear, stratification, and turbulence within a tropical instability wave cycle. *Journal of Geophysical Research: Oceans*, **124 (3)**, 1858–1875.

Johnson, G. C., M. J. McPhaden, and F. E, 2001: Equatorial pacific ocean horizontal velocity, divergence, and upwelling. *Journal of Physical Oceanography*, **31**, 839—-848.

Jong, B.-T., M. Ting, and R. Seager, 2016: El niño's impact on california precipitation: Seasonality, regionality, and el niño intensity. *Environmental Research Letters*, **11 (5)**, 054 021.

Kessler, W. S., 2006: The circulation of the eastern tropical pacific: A review. *Progress in Oceanography*, **69 (2-4)**, 181–217.

Klein, S. A., and D. L. Hartmann, 1993: The seasonal cycle of low stratiform clouds. *Journal of Climate*, **6 (8)**, 1587–1606.

Kobayashi, S., and Coauthors, 2015: The jra-55 reanalysis: General specifications and basic characteristics. *Journal of the Meteorological Society of Japan. Ser. II*, **93 (1)**, 5–48.

Legeckis, R., 1977: Long waves in the eastern equatorial pacific ocean: A view from a geostationary satellite. *Science*, **197 (4309)**, 1179–1181.

Lengaigne, M., U. Hausmann, G. Madec, C. Menkes, J. Vialard, and J. Molines, 2012: Mechanisms controlling warm water volume interannual variations in the equatorial pacific: diabatic versus adiabatic processes. *Climate Dynamics*, **38**, 1031–1046.

Lien, R.-C., E. A. d'Asaro, and C. E. Menkes, 2008: Modulation of equatorial turbulence by tropical instability waves. *Geophysical Research Letters*, **35 (24)**.

McPhaden, M. J., A. J. Busalacchi, and D. L. Anderson, 2010: A toga retrospective. *Oceanography*, **23 (3)**, 86–103.

McPhaden, M. J., and Coauthors, 1998: The tropical ocean-global atmosphere observing system: A decade of progress. *Journal of Geophysical Research: Oceans*, **103 (C7)**, 14 169–14 240.

Meinen, C., M. J. McPhaden, and G. C. Johnson, 2001: Vertical velocities and transports in the equatorial pacific during 1993-99. *Journal of Physical Oceanography*, **31**, 3230–3248.

Meinen, C. S., and M. J. McPhaden, 2000: Observations of warm water volume changes in the equatorial pacific and their relationship to el niño and la niña. *Journal of Climate*, **13 (20)**, 3551–3559.

Meinen, C. S., and M. J. McPhaden, 2001: Interannual variability in warm water volume transports in the equatorial pacific during 1993–99. *Journal of physical oceanography*, **31 (5)**, 1324–1345.

Miller, L., D. R. Watts, and M. Wimbush, 1985: Oscillations of dynamic topography in the eastern equatorial pacific. *Journal of physical oceanography*, **15 (12)**, 1759–1770.

Moum, J., R.-C. Lien, A. Perlin, J. Nash, M. Gregg, and P. Wiles, 2009: Sea surface cooling at the equator by subsurface mixing in tropical instability waves. *Nature Geoscience*, **2 (11)**, 761–765.

Moum, J. N., A. Perlin, J. D. Nash, and M. J. McPhaden, 2013: Seasonal sea surface cooling in the equatorial pacific cold tongue controlled by ocean mixing. *Nature*, **500 (7460)**, 64–67.

Niiler, P., and J. Stevenson, 1982: The heat budget of tropical ocean warm-water pools. *J. Mar. Res*, **40**, 465–480.

Nurser, A., R. Marsh, and R. G. Williams, 1999: Diagnosing water mass formation from air–sea fluxes and surface mixing. *Journal of physical oceanography*, **29 (7)**, 1468–1487.

Ohlmann, J. C., 2003: Ocean radiant heating in climate models. *Journal of Climate*, **16 (9)**, 1337–1351.

Perez, R. C., M. F. Cronin, and W. S. Kessler, 2010: Tropical cells and a secondary circulation near the northern front of the equatorial pacific cold tongue. *Journal of physical oceanography*, **40 (9)**, 2091–2106.

Qiao, L., and R. H. Weisberg, 1995: Tropical instability wave kinematics: Observations from the tropical instability wave experiment. *Journal of Geophysical Research: Oceans*, **100 (C5)**, 8677–8693.

Rai, S., M. Hecht, M. Maltrud, and H. Aluie, 2021: Scale of oceanic eddy killing by wind from global satellite observations. *Science Advances*, **7 (28)**, eabf4920, https://doi.org/10.1126/sciadv.abf4920.

Renault, L., S. Masson, T. Arsouze, G. Madec, and J. C. Mcwilliams, 2020: Recipes for how to force oceanic model dynamics. *Journal of Advances in Modeling Earth Systems*, **12 (2)**, e2019MS001 715.

Rocklin, M., 2015: Dask: Parallel computation with blocked algorithms and task scheduling. *Proceedings of the 14th python in science conference*, Citeseer, 130-136.

Smith, N., and Coauthors, 2019: Tropical pacific observing system. *Frontiers in Marine Science*, **6**, 31.

Smith, R., and Coauthors, 2010: The parallel ocean program (pop) reference manual: Ocean component of the community climate system model (ccsm). *Los Alamos Natl Lab LAUR-10-01853*.

Smyth, W., and J. Moum, 2013: Marginal instability and deep cycle turbulence in the eastern equatorial pacific ocean. *Geophysical Research Letters*, **40 (23)**, 6181–6185.

Smyth, W., J. Moum, L. Li, and S. Thorpe, 2013: Diurnal shear instability, the descent of the surface shear layer, and the deep cycle of equatorial turbulence. *Journal of Physical Oceanography*, **43 (11)**, 2432–2455.

Sun, C., W. D. Smyth, and J. N. Moum, 1998: Dynamic instability of stratified shear flow in the upper equatorial pacific. *Journal of Geophysical Research: Oceans*, **103 (C5)**, 10 323–10 337.

Sun, Z., H. Liu, P. Lin, Y.-h. Tseng, J. Small, and F. Bryan, 2019: The modeling of the north equatorial countercurrent in the community earth system model and its oceanic component. *Journal of Advances in Modeling Earth Systems*, **11 (2)**, 531–544, https://doi.org/https://doi.org/10.1029/2018MS001521, URL https://agupubs.onlinelibrary.wiley.com/doi/abs/10.1029/2018MS001521, https://agupubs.onlinelibrary.wiley.com/doi/pdf/10.1029/2018MS001521.

Toole, J. M., H.-M. Zhang, and M. J. Caruso, 2004: Time-dependent internal energy budgets of the tropical warm water pools. *Journal of climate*, **17 (6)**, 1398–1410.

Tsujino, H., and Coauthors, 2018: Jra-55 based surface dataset for driving ocean–sea-ice models (jra55-do). *Ocean Modelling*, **130**, 79–139.

Walin, G., 1982: On the relation between sea-surface heat flow and thermal circulation in the ocean. *Tellus*, **34**, 187–195.

Wang, W., and M. J. McPhaden, 1999: The surface-layer heat balance in the equatorial pacific ocean. part i: Mean seasonal cycle. *Journal of physical oceanography*, **29 (8)**, 1812–1831.

Warner, S. J., and J. N. Moum, 2019: Feedback of mixing to enso phase change. *Geophysical Research Letters*, **46 (23)**, 13 920–13 927.

Weisberg, R. H., and L. Qiao, 2000: Equatorial upwelling in the central pacific estimated from moored velocity profilers. *Journal of Physical Oceanography*, **30 (1)**, 105–124.

Willett, C. S., R. R. Leben, and M. F. Lavín, 2006: Eddies and tropical instability waves in the eastern tropical pacific: A review. *Progress in Oceanography*, **69 (2-4)**, 218–238.

Wyrtki, K., 1981: An estimate of equatorial upwelling in the pacific. *Journal of Physical Oceanography*, **11**, 1205–1214.

Xu, H., S.-P. Xie, and Y. Wang, 2005: Subseasonal variability of the southeast pacific stratus cloud deck. *Journal of climate*, **18 (1)**, 131–142.

Yeh, S.-W., and Coauthors, 2018: Enso atmospheric teleconnections and their response to greenhouse gas forcing. *Reviews of Geophysics*, **56 (1)**, 185–206.

Yu, J.-Y., and C. R. Mechoso, 1999: Links between annual variations of peruvian stratocumulus clouds and of sst in the eastern equatorial pacific. *Journal of Climate*, **12 (11)**, 3305–3318.